ZIPPER GRIDS FOR FORCE AND MOMENT COMPUTATION ON OVERSET GRIDS

William M. Chan * and Pieter G. Buning †
NASA-Ames Research Center
Mail Stop T27B-2
Moffett Field, California 94035-1000

Abstract

A scheme is developed to account for the overlapped zones on overset structured surface grids when computing forces and moments for the surface. Grid points in the overlapped zone between grids are blanked. The resulting gaps are then filled by 'zipper grids' which are strings of triangular cells that conform to the original surface. A hybrid composite surface grid is formed which consists of non-overlapping quadrilaterals and triangles, where the quadrilaterals are the unblanked cells in the original surface grids and the triangles are the newly generated triangular cells in the gaps. Pressure and viscous stresses which are known at the grid points can then be integrated accurately on the hybrid surface. Results obtained by applying the current scheme to numerical solutions are compared with data from wind tunnel tests for several complex configurations. These include the Space Shuttle Launch Vehicle, a subsonic transport, and a supersonic oblique all-wing configuration.

1. Introduction

Chimera overset grid methods[1] have been successfully applied in the numerical flow simulations of complex configurations such as the Space Shuttle Launch Vehicle,[2,3,4] the V-22 tiltrotor,[5] the SOFIA Airborne Observatory,[6] and many others. Very good agreement of many flow characteristics has been obtained between the numerical solution and wind tunnel/flight tests. One of the most important set of quantities sought from numerical solutions is the set of force and moment coefficients for the solid surfaces in the flow field. Accurate computation of these quantities is crucial for study of aerodynamics, design optimization, and moving body problems.

Forces and moments are usually computed by integrating the pressure and viscous stresses on the surface grids. Since the surface grids for overset grids are allowed to overlap arbitrarily, the regions in the overlapped zones are counted more than once if integration is performed over all the surface grids. In order for overset grid methods to be widely accepted for use in practical applications, a scheme must be available to accurately extract force and moment information from the numerical solutions. A procedure developed to solve this problem is described in this paper.

The method for computing force and moment coefficients is broken into two main steps performed by two separate computer codes. The first step is to construct a hybrid composite surface grid consisting of non-overlapping quadrilaterals (quads) and triangles (the MIXSUR code), while the second step is to integrate the pressure and viscous stresses on the hybrid grid (the OVERINT code). Generation of the hybrid composite surface grid only needs to be performed once before the flow solver is called. Integration of pressure and viscous stresses can be performed just once at the end of the run to compute the final force and moment coefficients. It can also be performed every N number of iterations to supply the force and moment coefficients as indicators of convergence, or as input to a six-degrees-of-freedom rigid body dynamics package for moving body applications. In both cases, the connections between the quads and the triangles in the hybrid composite surface grid do not change with iterations.

Steps involved in the generation of the hybrid grid are described in §2. The integration scheme is presented in §3. In §4, the results of applying the current scheme on numerical solutions are compared with data obtained in wind tunnel tests, and results from using an alternative force/moment computation scheme.[4] Summary and conclusions are given in §5.

---

* Research Scientist, MCAT, Inc., Member AIAA.
† Research Scientist, NASA Ames Research Center, Senior Member AIAA

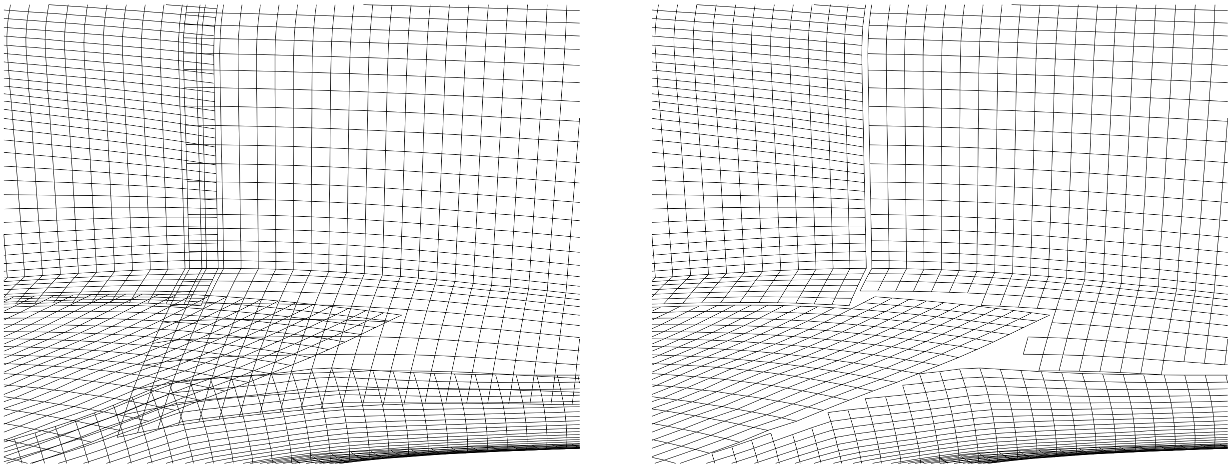
(a) (b)

Figure 1. (a) Surface grids for four overlapping subsets. (b) Surface grids after blanking of points in overlapped regions.

2. Hybrid Composite Grid Generation

An overset grid system consists of a collection of overlapping volume grids together with information on inter-grid connectivity. Let J, K and L be the grid indices of a typical volume grid. The surface domain on which forces and moments are to be computed can be described by a collection of surface subsets. Each surface subset is a subset of a J, K or L = constant slice of a volume grid in the system. For the rest of this paper, a surface subset will be referred to as a subset for short. An example with four overlapping subsets is shown in Figure 1a. A hybrid composite grid will be generated from the collection of subsets. This procedure consists of the following three main automated steps which are described in more detail in the subsections below.

(a) Points in the overlapped regions between subsets are blanked resulting in gaps between subsets. For any overlapping pair of subsets, only points from the coarser of the two subsets are blanked.

(b) Points on the boundaries of the gaps are identified and ordered. This creates a collection of strings of gap boundary points.

(c) Matching pairs of strings of gap boundary points are connected to form a zipper grid which is a single layer of triangular cells that fills the gap between neighboring subsets and conforms to the original surface. In regions where more than two subsets overlap, multiple zipper grids are allowed to converge in a pocket of triangular cells.

An alternative to the above procedure is to retain all the points in all the subsets including those in the overlapped zones and then perform triangulation over the entire surface domain.[7] We have chosen not to do this for the following reason. If there are flow gradients not fully resolved by neighboring grids in the overlapped region, the solution will differ slightly. Use of points from all neighboring grids in this region would result in integration of an unsmooth pressure and/or viscous stress field. Although the hybrid grid generation procedure is more complex in the zipper grid approach, the effect of any solution mismatches is minimized by keeping as many non-overlapping quads as possible and introducing just a single layer of triangular cells. For conservation purposes, hybrid grids have also been used to replace overlapping structured grids in a 2-D or 3-D domain.[8] In that approach, all points in the overlapped region are blanked and the entire overlapped region is triangulated.

2.1. *Grid Point Blanking Scheme in Overlapped Zone*

The integration of forces and moments is performed on the set of non-overlapping quads and triangular cells. The set of non-overlapping quads is derived from the defined subsets where some of the points are blanked to ensure that the quads do not overlap. This information is stored in an integration iblank variable $B_{j,k}$ for each point on the subsets, where $B_{j,k}$ is defined by

$$B_{j,k} = \begin{cases} 1, & \text{if point is used for integration;} \\ 0, & \text{if point is not used for integration,} \end{cases} \tag{2.1}$$

and j, k are grid indices for a subset. A quad is integrated if all four of its vertices have $B_{j,k} = 1$.

Initially, $B_{j,k}$ is set to the value 1 for all points on the subsets. Any point that is a hole point as a result of Chimera inter-grid connectivity[1] will have $B_{j,k}$ set to 0. Points in the overlapped region between subsets are then identified. For any pair of subsets that overlap, grid points on the coarser of the two subsets are blanked, i.e. $B_{j,k}$ set to 0. The coarser subset is defined to be the one with the fewer grid points in the overlapped region.

Points are identified to be inside an overlapped zone by a 'minmax' box approach.[9] A minmax box is a collection of 6 numbers that indicates the smallest and largest x, y and z coordinates of the objects enclosed. A big minmax box is defined for each subset and small minmax boxes are defined for each quad of each subset. Then the blanking procedure goes as follows.

(1) Let S_i and S_j be any two subsets. Given a point in S_i, the big minmax box of S_j is used to quickly determine whether the point falls inside of S_j. If it does, then the small minmax boxes of S_j are used to determine whether the point falls inside any quad in S_j. If such a quad is found, then the point is counted as falling in the overlapped zone between S_i and S_j.

(2) The number of points in S_i that falls in the overlapped zone with S_j is computed and stored in $N(S_i, S_j)$. Similarly, $N(S_j, S_i)$ is also computed.

(3) If $N(S_i, S_j) \leq N(S_j, S_i)$, then all the points in S_i that fall in the overlapped zone with S_j are blanked. This guarantees that all unblanked points in S_i are not contained in any quad in S_j. However, the reverse is not necessarily true. Hence, a further test is necessary to blank any unblanked points of S_j that fall inside an unblanked quad in S_i. The procedure follows similarly with the role of S_i and S_j reversed if $N(S_j, S_i) < N(S_i, S_j)$.

(4) This is performed for all pairs of subsets.

(5) After all the blanking is completed, some loose strings of unblanked points may remain which are surrounded by blanked points. A final test is then performed to blank out these loose strings of points.

Figure 1b shows the remaining non-overlapping quads after the blanking step is performed on the example in Figure 1a. Since the surface grid lines are generally not aligned with the Cartesian coordinate axes, the use of minmax boxes will tend to blank out more points than is necessary. A more accurate but also more expensive test could be used to reduce the size of the gaps created.

2.2. *Stringing of Gap Boundary Points*

The second step in the hybrid grid generation procedure is to identify and order the points on the gap boundaries created by the blanking step. These points fall under two types: (I) points on the boundary of holes defined by the integration iblank variable, and (II) points on the boundary of subsets that lie in the overlapped region with another subset.

Type I points are identified by examining $B_{j,k}$. First, it must be an unblanked point. For an interior point (j,k) to qualify as a Type I point, at least 3 and no more than 7 of its 8 neighboring points must be unblanked. The neighboring points are located at $(j-1,k-1)$, $(j-1,k)$, $(j+1,k)$, $(j,k-1)$, $(j,k+1)$, $(j-1,k+1)$, $(j,k+1)$ and $(j+1,k+1)$. For a point on the boundary or a corner of a subset, it is a Type I point if any one of its 3 or 2 neighbors are blanked, respectively. Type II points are identified by testing if any boundary points on a given subset lie inside any small minmax box of a cell from another subset.

After identifying the gap boundary points, they need to be connected to form ordered strings of points. Two gap boundary points are connected if an edge of a subset exists between them. The connection of the gap boundary points then results in a collection of gap boundary strings (see Figure 1c).

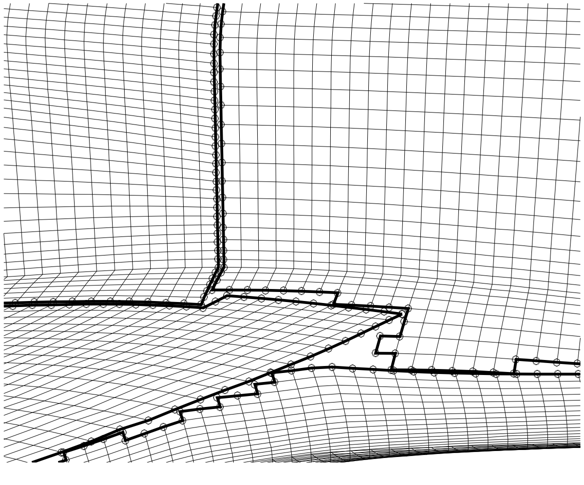

Figure 1. (c) Points on gap boundary strings are indicated by circles joined by thick lines.

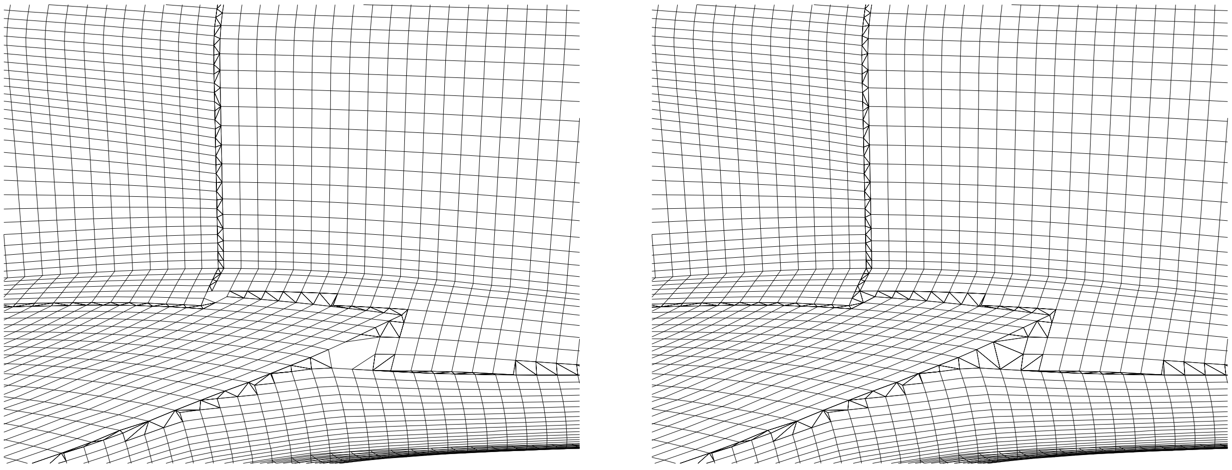

(d) (e)

Figure 1. (d) Gaps between pairs of boundary segments are filled by zipper grids where each consists of a single layer of triangular cells. (e) Final hybrid composite surface grid with remaining polygonal gaps filled with triangles.

2.3. *Construction of Zipper Grids*

Triangles are constructed by connecting points between pairs of gap boundary strings resulting in a set of zipper grids. Each zipper grid is a single layer of triangular cells. No new points are introduced in the generation of these cells which are required to conform to the original surface geometry. The steps involved in this procedure are described below.

2.3.1. *Boundary Segment Matching*

A zipper grid is formed by connecting points between segments of two boundary strings. Each boundary string R_i is divided into segments as follows. For each point P_i on R_i, the nearest point on another boundary string R_j is located. The point P_i is now mapped to the boundary string R_j. A segment of R_i is a set of contiguous points on R_i that is mapped to R_j. A segment from R_i that is mapped to R_j is matched with a segment from R_j that is mapped to R_i.

2.3.2. *Zipping*

The matching step identifies segment pairs that should be connected via a zipper grid. Let A and B be a segment pair to be connected. The algorithm used to construct a zipper grid is as follows.

(a) *Selection of initial points*

The first connection between A and B is formed by searching for a starting point in A and a starting point in B to connect to each other. For a non-periodic segment pair A and B, the two end points of segment A and B that are closest to each other are chosen as the starting points of the zipping process. For a periodic segment pair A and B, any two closest points between the two segments can be used as starting points.

(b) *Connection to form triangles*

Let P_i be the ith point on segment A and P_j be the jth point on segment B where $i = j = 1$ at the starting points. Also let $i_{\max}$, and $j_{\max}$ be the number of points on A and B, respectively. For $i < i_{\max}$ and $j < j_{\max}$, P_i may be connected to P_{j+1} or P_j may be connected to P_{i+1}. The first step is to test if the quad formed by the points P_i, P_{i+1}, P_{j+1} and P_j is convex. The connection of P_i to P_{j+1} splits the quad into two triangles. If the normals of these triangles have the same sign, then the connection is valid. A similar test is performed for the P_j to P_{i+1} connection. In cases where only one of the two connections is valid, the valid connection is chosen. In cases where both connections are valid, the quad is convex and the connection with the shortest distance is chosen. However, if both connections are invalid, the quad is crossed inside out. The shortest distance test is still performed and can result in good triangulations in some situations. When bad triangulations are obtained, we will proceed to the next connection but the bad triangles are flagged. When $i = i_{\max}$ is reached (last point of segment A), all remaining points in segment B are connected to the last point in segment A, and vice versa.

(c) *Reconnection to remove bad triangles*

When there is a large discrepancy between the grid resolutions of the neighboring grids in the overlapped zone, and when the grid lines are not aligned, the zipping procedure described above can sometimes produce bad triangles. These triangles are bad in the sense that they overlap some existing quad or good triangle. From experience, typically only less than 1% of the triangles created are bad under the conditions stated above. Some of these bad triangles can be removed and good triangles can be formed by performing the zipping step (b) in the reverse direction in the region of bad triangles. Zipper grids for the example started in §2.1 are shown in Figure 1d.

2.3.3. *Closing of Pockets*

After connecting pairs of gap boundary segments, most of the gaps created by the blanking procedure described in §2.1 are now closed by triangular cells. However, there may be small gaps left in regions where three or more subsets overlap. Each small gap is in the form of a closed polygon where each edge of the boundary is either an unconnected edge of a gap boundary segment or an end edge of one of the zipper grids. These edges are identified and connected to form a closed loop. The gap inside the closed loop is then triangulated without introducing new points using a similar zipping algorithm as described in the previous subsection. First, a starting edge has to be chosen. This is selected to be the edge whose end points contain interior angles that are closest to 90 degress. Zipping then proceeds from the starting edge until the entire polygon is filled with triangles. The complete hybrid composite grid for the example started in §2.1 is shown in Figure 1e.

3. Pressure and Viscous Stress Integration

Integration of the pressure and viscous stresses is performed on the hybrid composite surface consisting of a collection of non-overlapping quadrilaterals and triangles. For each quadrilateral or triangle, the value of the function being integrated is known at the vertices. A number of quadrature rules can be used to perform the integration. For simplicity, the function is assumed to be a constant inside the area of the quadrilateral or triangle where the constant is the arithmetic average of the values of the function at the vertices. This can be written as

$$\int_{polygon} f\, d\vec{A} \approx \left(\frac{1}{N_v} \sum_{i=1}^{Nv} f_i \right) \cdot \vec{n} \Delta A, \qquad (3.1)$$

where f is a scalar function to be integrated, *polygon* is either a quadrilateral or a triangle, N_v is the number of vertices of the polygon, f_i is the value of the scalar function at the vertices, $\vec{n}$ is the unit normal of the polygon, and ΔA is the area of the polygon. A similar expression can be written for the integral of a vector function $\vec{f}$. For a triangle, the normal is uniquely defined. For a quad, the normal is computed by the cross product of the diagonals. The integral in (3.1) is performed over all the unblanked quads and triangles and the results are summed and normalized to obtain the force and moment coefficients.

There are three possible ways to perform the quadrature over a quad by treating it as (1) a 4-point polygon, (2) two triangles by connecting one diagonal of the quad, (3) two triangles by connecting the other diagonal of the quad. Let I_q, I_{t1} and I_{t2} be the value of the integral computed using options (1), (2) and (3), respectively. It can be shown analytically that if the quadrature rule given by (3.1) is used on a parallelogram, then

$$I_{t1} \leq I_q \leq I_{t2}. \qquad (3.1)$$

Hence, for a quad that is a parallelogram, option (1) is the better choice since options (2) and (3) tend to produce undesirable biases. However, as a quad degenerates to a triangle as in the case of two adjacent points becoming very close together, option (2) or (3) is more attractive since the two close points are not counted twice. On typical surface grids for CFD applications, most of the quads are approximately parallelograms in shape. We have therefore chosen option (1) for the quadrature on quads. Cells adjacent to a singular axis point on a surface subset are integrated as triangles.

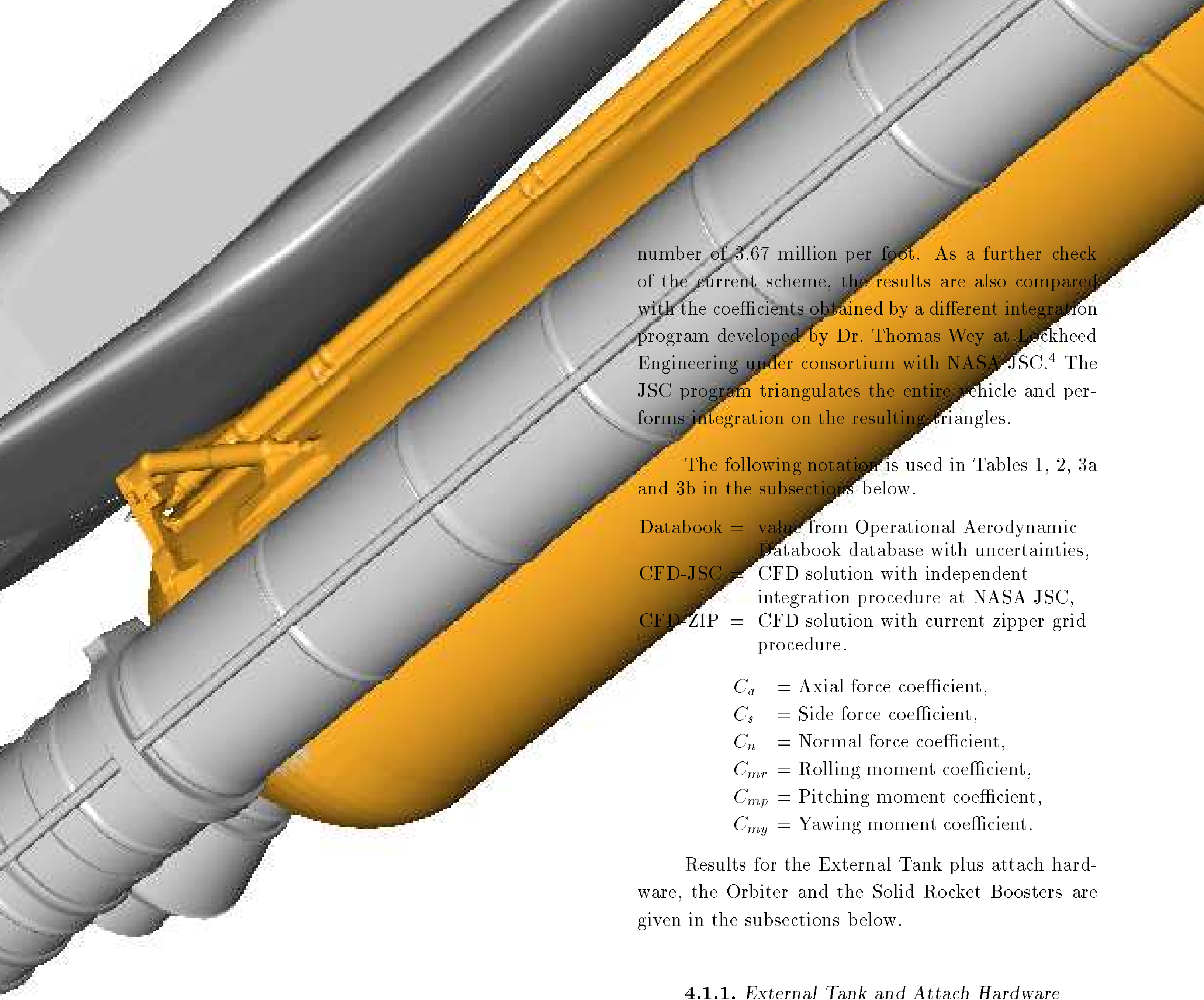

Figure 2. Components of the Space Shuttle Launch Vehicle.

The highly complex configuration of the Space Shuttle Launch Vehicle[2,3,4] (see Figure 2) offers a good test bed for the scheme described in this paper. The overset grid system contains 113 grids and 16.4 million grid points. Numerical solutions were computed by the Ascent Wing Aerodynamic Loads Verification Team at NASA Johnson Space Center (JSC) using the Chimera Navier-Stokes flow solver OVERFLOW.[10] In addition, wind tunnel measurements are available where the data is compiled and recorded in a data base - the Operational Aerodynamic Databook (OADB) database.[11] Although measurements were carried out under wind tunnel Reynolds numbers, the data has been adjusted using flight measurements to allow predictions for flight Reynolds numbers. This data is compared with the coefficients obtained using the scheme described in this paper applied to a CFD solution at a Mach number of 1.05, angle of attack of -3.08 degrees, and a Reynolds number of 3.67 million per foot. As a further check of the current scheme, the results are also compared with the coefficients obtained by a different integration program developed by Dr. Thomas Wey at Lockheed Engineering under consortium with NASA JSC.[4] The JSC program triangulates the entire vehicle and performs integration on the resulting triangles.

The following notation is used in Tables 1, 2, 3a and 3b in the subsections below.

Databook = value from Operational Aerodynamic Databook database with uncertainties,
CFD-JSC = CFD solution with independent integration procedure at NASA JSC,
CFD-ZIP = CFD solution with current zipper grid procedure.

C_a = Axial force coefficient,
C_s = Side force coefficient,
C_n = Normal force coefficient,
C_{mr} = Rolling moment coefficient,
C_{mp} = Pitching moment coefficient,
C_{my} = Yawing moment coefficient.

Results for the External Tank plus attach hardware, the Orbiter and the Solid Rocket Boosters are given in the subsections below.

4.1.1. *External Tank and Attach Hardware*

Databook values are available for the combined External Tank (ET) and the Orbiter/ET attach hardware. The first comparison is performed on this combination. Zipper grids generated in the forward attach hardware region and the base region of the ET are shown in Figures 3a and 3b. Excellent agreement is obtained in the comparison of force and moment coefficients between Databook, CFD-JSC and CFD-ZIP data given in Table 1.

Coefs	Databook	CFD-JSC	CFD-ZIP
C_a	0.1591 ± 0.0319	0.1339	0.1375
C_s	0.0027 ± 0.0119	0.0026	0.0026
C_n	-0.1438 ± 0.0145	-0.1472	-0.1474
C_{mr}	-0.0005 ± 0.0016	-0.0001	0.0000
C_{mp}	0.0351 ± 0.0097	0.0273	0.0350
C_{my}	0.0025 ± 0.0067	0.0016	0.0021

Table 1. Force and moment coefficients for the External Tank and the Orbiter/ET attach hardware combined.

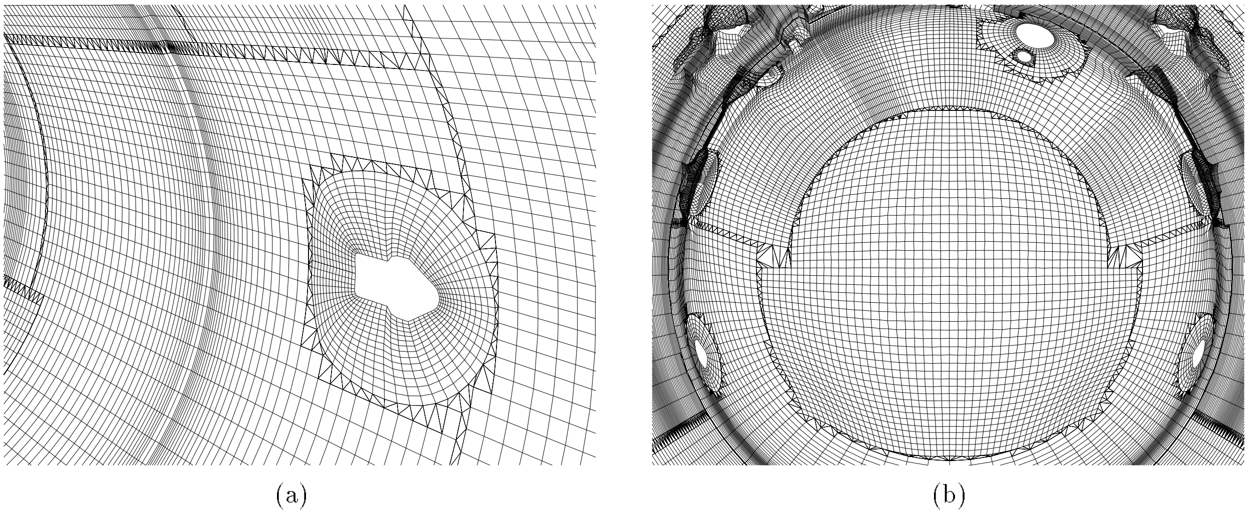
(a) (b)

Figure 3. Hybrid composite surface grids for the External Tank in the (a) forward attach hardware region, (b) base region looking from interior of tank to downstream.

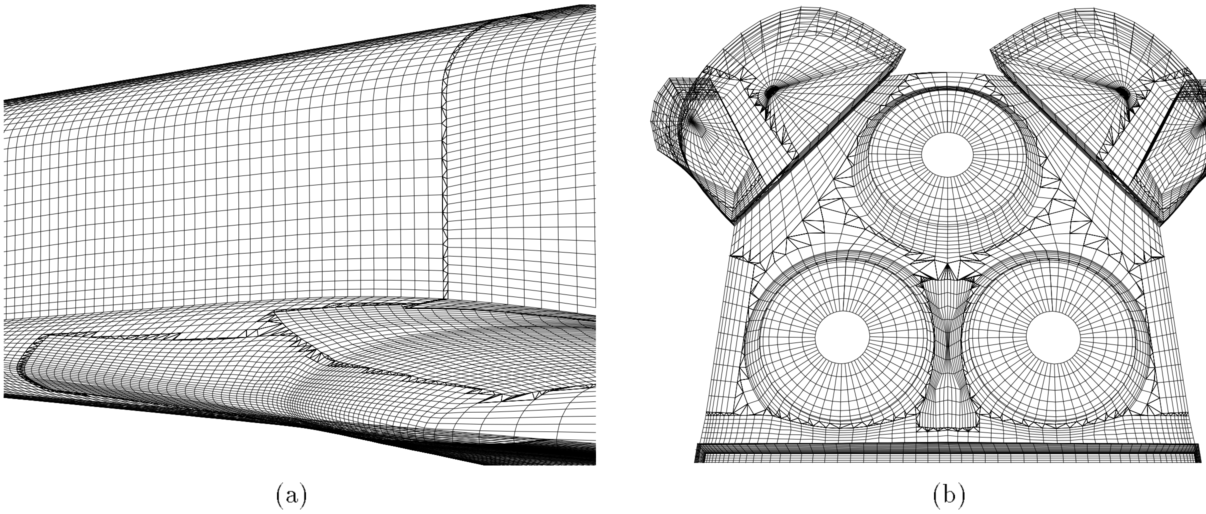
(a) (b)

Figure 4. Hybrid composite surface grids for the Orbiter in the (a) wing leading edge region, (b) base region (nozzles not shown).

4.1.2. *Orbiter*

The second comparison is performed on the Orbiter. Zipper grids for the fuselage/wing region and the base region are shown in Figures 4a and 4b, respectively. Comparisons with the Databook values and the JSC integration procedure are presented in Table 2. The results obtained using the current scheme are close to those obtained by the independent JSC integration program which shows that the procedure described in this paper is working fine. Discrepancies with the Databook values are probably caused by incomplete modelling of the physics by the flow solver, and difficulties in interpreting the uncertainty bounds in the Databook.

Coefs	Databook	CFD-JSC	CFD-ZIP
C_a	0.0820 ± 0.0161	0.1101	0.1086
C_s	0.0019 ± 0.0100	0.0004	0.0006
C_n	0.0753 ± 0.0267	0.1023	0.0990
C_{mr}	0.0015 ± 0.0038	-0.0007	-0.0006
C_{mp}	-0.0341 ± 0.0205	-0.0537	-0.0499
C_{my}	-0.0035 ± 0.0075	0.0005	0.0007

Table 2. Force and moment coefficients for the Orbiter.

4.1.3. *Solid Rocket Boosters*

The next comparison is performed on the Left and Right Solid Rocket Boosters. Force and moment coefficients are given in Table 3a and 3b. Again, good agreement is obtained between the CFD-JSC results and the CFD-ZIP results.

Coefs	Databook	CFD-JSC	CFD-ZIP
C_a	0.0349 ± 0.0128	0.0357	0.0348
C_s	0.0265 ± 0.0123	0.0051	0.0007
C_n	-0.0294 ± 0.0103	−0.0306	−0.0308
C_{mr}	-0.0054 ± 0.0018	0.0060	0.0060
C_{mp}	0.0034 ± 0.0086	0.0064	0.0066
C_{my}	-0.0386 ± 0.0094	0.0131	0.0124

Table 3a. Force and moment coefficients for the Left Solid Rocket Booster.

Coefs	Databook	CFD-JSC	CFD-ZIP
C_a	0.0348 ± 0.0128	0.0354	0.0343
C_s	-0.0257 ± 0.0123	−0.0051	−0.0009
C_n	-0.0278 ± 0.0103	−0.0289	−0.0294
C_{mr}	0.0051 ± 0.0018	−0.0056	−0.0058
C_{mp}	0.0005 ± 0.0086	0.0047	0.0052
C_{my}	0.0390 ± 0.0094	−0.0132	−0.0126

Table 3b. Force and moment coefficients for the Right Solid Rocket Booster.

4.2. *Subsonic Transport Configuration*

This test case involves a subsonic transport configuration where the data was supplied by Dr. Lie-Mine Gea.[12] The geometry consists of a fuselage, wing, pylon, nacelle, and cowl (see Figure 5). The overset grid system is composed of grids for the above components together with collar grids for the pylon/wing junction, pylon/nacelle junction, and the pylon/cowl junction. A numerical solution at a Mach number of 0.85 was obtained using the flow solver OVERFLOW[10]. Zipper grids generated for some of the regions are shown in Figure 6a,b. Force coefficients are computed by applying the procedure described in this paper on the numerical solution. Comparisons are made with data obtained from wind tunnel tests performed at the Langley 16-Foot Transonic Wind Tunnel. For a lift coefficient of 0.61, the drag coefficient from the CFD computation is lower than the wind tunnel data by 0.0036. However, an inviscid wall was assumed for the fuselage in the CFD run. After an adjustment is made to the fuselage drag using flat plate analysis, the drag coefficient from the CFD computation is higher than the wind tunnel data by 0.0024.

Figure 5. Surface geometry of subsonic transport configuration.

4.3. *Supersonic Oblique All-Wing Configuration*

A supersonic oblique all-wing configuration was tested in the NASA Ames 9- by 7-Foot Supersonic Wind Tunnel in 1994. The design and testing of this configuration was a cooperative effort between McDonnell Douglas, Boeing, and NASA Ames Research Center. CFD computations were performed to determine model support interference and for real-time comparison with pressure sensitive paint images generated during the test. Earlier CFD computations were performed for a wing alone case.[13] As shown in Figure 7a, current CFD simulations using OVERFLOW[10] included the oblique wing, vertical tails, pylons with flow-through nacelles, and a model support blade. On the wind tunnel model, boundary layers were tripped near the leading edge of all components. For the CFD simulations, viscous surfaces which consisted of the wing and vertical tails were considered fully turbulent.

The grid system included 6 million points in 53 grids. This grid density was driven both by the need to resolve flow gradients generated by the various components and by the requirement for good boundary communication between the overlapping grids. A close-up view of the lower wing surface in Figure 7b shows the surface grids and zipper grids around the model support blade and several of the pylons. Since the pylons and nacelles were simulated as inviscid surfaces, a flat plate drag correction was added to the computed drag

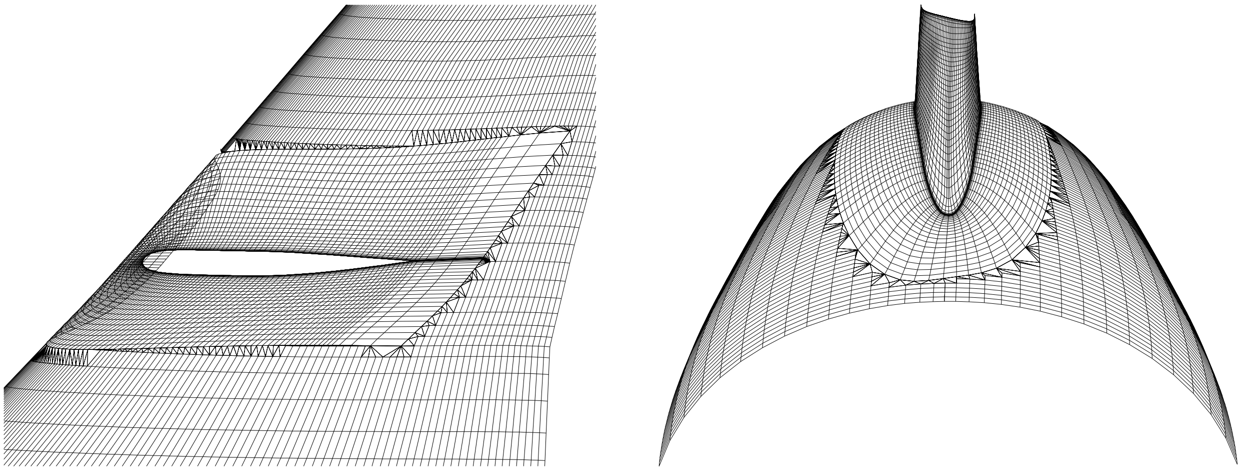

(a) (b)

Figure 6. (a) Hybrid composite surface grid in the lower wing and the pylon/wing collar grid region (top view). Part of the pylon/wing collar surface grid wraps over the leading edge of the wing as shown. (b) Hybrid composite surface grid in the upper outer nacelle and pylon/nacelle collar grid region.

numbers for these surfaces. The inner nacelles were treated appropriately to be consistent with the methods used to obtain the wind tunnel results.

Comparisons of wind tunnel and computed force coefficients from the CFD solution are presented in Figure 8a-c for an alpha sweep at Mach 1.6 and a Reynolds number of 3 million per foot. Excellent agreement is obtained through much of the alpha range for all six degrees of freedom. For the moment coefficients (not presented here), some anomalous behavior is obtained at the high angles of attack. While the purpose of this paper is not to validate the CFD approach, this agreement does demonstrate the applicability of the force integration approach given an accurate CFD simulation.

5. Summary and Conclusions

A critical missing piece of technology for overset grid methods has been filled by the development of a scheme to account for the overlapped zones when computing force and moment coefficients on overset surface grids. Two computer codes were developed to perform the two main steps of the force and moment computation procedure: MIXSUR to generate the hybrid composite surface grid and OVERINT to perform the integration. A simple quadrature rule is used to perform the integration on the hybrid composite surface grid which consists of non-overlapping quads and triangles that conform to the original surface. Very good comparison was obtained between data extracted from numerical solutions and wind tunnel tests for various complex configurations.

Acknowledgements

The authors would like to thank Mr. Jeff Slotnick of Lockheed Engineering Sciences Company and Mr. Ray Gomez of NASA Johnson Space Center for many detailed discussions on the Space Shuttle Launch Vehicle computations and for providing the corresponding data sets. Data for the subsonic transport configuration was kindly supplied by Dr. Lie-Mine Gea of McDonnell Douglas Aerospace-West. The authors would also like to thank Mr. Robert Kennelly of NASA Ames and Mr. Christopher Lee of MCAT, Inc. for processing and supplying data for the Oblique All-Wing configuration. This work is sponsored in part by the Space Shuttle Engineering Integration Office at NASA Johnson Space Center via NASA Ames Research Center, and in part by the Advanced Subsonic Technology Program at NASA Ames Research Center. The first author was employed by MCAT Institute for most of this work under consortium number NCC2-654, and is currently employed by MCAT, Inc.

References

1. Steger, J. L., Dougherty, F. C. and Benek, J. A., "A Chimera Grid Scheme," *Advances in Grid Generation*, K. N. Ghia and U. Ghia, eds., ASME FED-Vol. 5, June, 1983.

2. Gomez, R. J. and Ma, E. C., "Validation of a Large Scale Chimera Grid System for the Space Shuttle Launch Vehicle," AIAA Paper 94-1859, *Proceedings of the AIAA 12th Applied Aerodynamics Conference,* Colorado Springs, CO, June, 1994.

3. Slotnick, J. P., Kandula, M. and Buning, P. G., "Navier-Stokes Simulation of the Space Shuttle Launch Vehicle Flight Transonic Flowfield Using a Large Scale Chimera Grid System," AIAA Paper 94-1860, *Proceedings of the AIAA 12th Applied Aerodynamics Conference,* Colorado Springs, CO, June, 1994.

4. Martin, F. W., Labbe, S., Pearce, D. G. and Wey, T. C., "Space Shuttle Launch Vehicle Wind Tunnel and Flight Aerodynamic Environments," AIAA Paper 94-1861, June, 1994.

5. Meakin, R., "Moving Body Overset Grid Methods for Complete Aircraft Tiltrotor Simulations," AIAA Paper 93-3350, *Proceedings of the AIAA 11th Computational Fluid Dynamics Conference,* Orlando, Florida, July, 1993.

6. Atwood, C. A. and Van Dalsem, W. R., "Flowfield Simulation about the SOFIA Airborne Observatory," AIAA Paper 92-0656, January, 1992.

7. Dietz, W. E., "General Approach to Calculating Forces and Moments on Overset Grid Configurations," *Proceedings of the 2nd Overset Composite Grid and Solution Technology Symposium*, Northwest Florida Section of AIAA, Fort Walton Beach, Florida, October, 1994.

8. Kao, K-H., Liou, M-S., "Direct Replacement of Arbitrary Grid-Overlapping by Nonstructured Grid," AIAA Paper 95-0346, January, 1995.

9. Chiu, I. T. and Meakin, R., "On Automating Domain Connectivity for Overset Grids," AIAA Paper 95-0854, AIAA 33rd Aerospace Sciences Meeting, January, 1995.

10. Buning, P. G., Chan, W. M., Renze, K. J., Sondak, D., Chiu, I. T. and Slotnick, J. P., "OVERFLOW User's Manual, Version 1.6ap", NASA Ames Research Center, Moffett Field, CA, 1994.

11. "Operational Aerodynamic Databook," Rockwell Document STS85-0118 CHG. 4, Rockwell Space Systems Division, Downey, California, January, 1992.

12. Gea, L. M., Halsey, N. D., Intemann, G. A. and Buning, P. G., "Applications of the 3-D Navier-Stokes Code OVERFLOW for Analyzing Propulsion-Airframe Integration Related Issues on Subsonic Transports," ICAS Paper 94-3.7.4, 19th Congress of the International Council of the Aeronautical Sciences, September, 1994.

13. Cheung, S., "Viscous CFD Analysis and Optimization of an Oblique All-Wing Transport," NASA CDCR-20005, November, 1994.

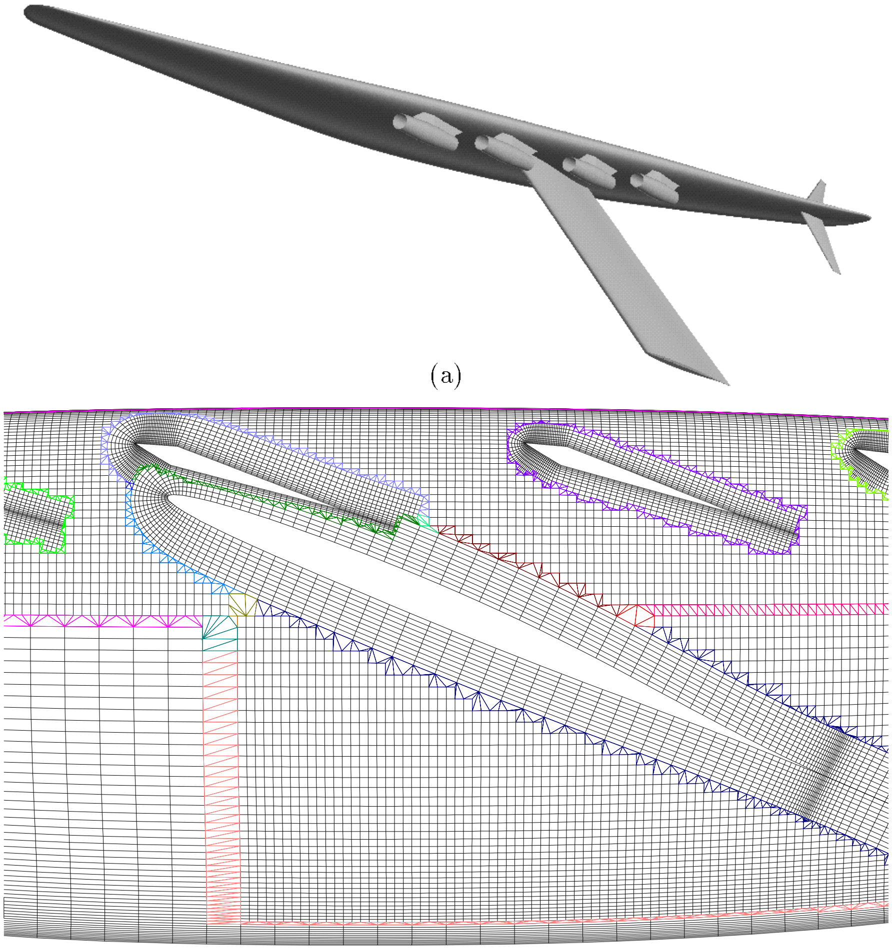

(a)

(b)

Figure 7. (a) Surface geometry of supersonic oblique all-wing configuration with model support blade. (b) Hybrid composite surface grid for region around model support blade and several of the pylons.

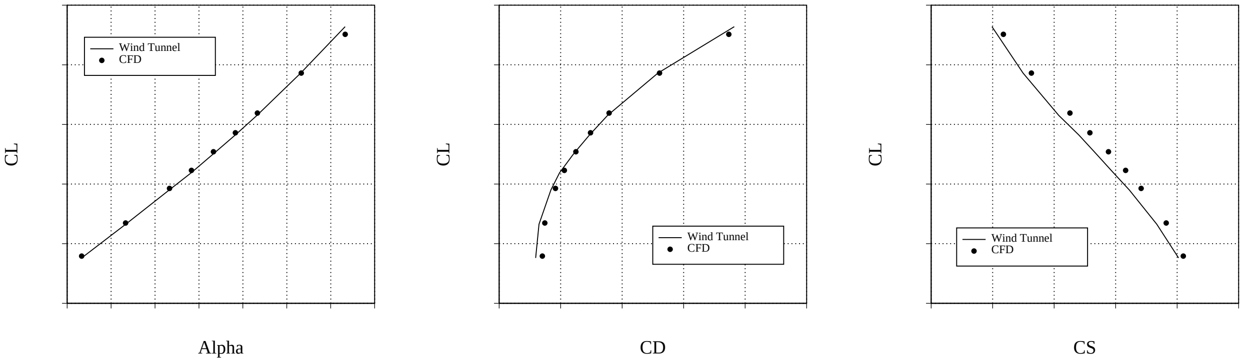

(a) (b) (c)

Figure 8. Comparison of wind tunnel data and computed force coefficients from CFD solution. (a) Lift versus angle of attack. (b) Lift versus drag. (c) Lift versus side force (Increments: CL=0.05, alpha=1 degree, CD=0.005, CS=0.01).